

## Article

# Seasonal and Interannual Variability of EAPE in the South China Sea Derived from ECCO2 Data from 1997 to 2019

Qiang Li <sup>1,2</sup>, Lei Zhou <sup>3</sup>  and Lingling Xie <sup>1,2,\*</sup>

<sup>1</sup> College of Ocean and Meteorology, Guangdong Ocean University, Zhanjiang 524088, China; liqiang@gdou.edu.cn

<sup>2</sup> Key Laboratory of Climate, Resources and Environment in Shelf Sea and Deep Ocean, Guangdong Ocean University, Zhanjiang 524088, China

<sup>3</sup> School of Oceanography, Shanghai Jiao Tong University, Shanghai 200240, China; zhoulei1588@sjtu.edu.cn

\* Correspondence: xiell@gdou.edu.cn

**Abstract:** Using Estimating the Circulation and Climate of the Ocean (phase 2, ECCO2) reanalysis products from 1997 to 2019, this study analyzes the spatiotemporal features of the eddy available gravitational potential energy (EAPE) in the South China Sea (SCS). The results indicate that the EAPE accounts for 64% of the total APE in the SCS with the climatological mean. The 2D EAPE distribution images manifest show high-value regions which are generally consistent with the eddy distributions. One region is located around 21° N and west of the Luzon Strait, the second around 17° N and near Luzon Island, and the third off the Vietnam coast. In the region around 21° N and 17° N, both the seasonal variability and the interannual variability associated with the El Niño–Southern Oscillation (ENSO) are significant. Off the Vietnam coast, the EAPE is closely associated with coastal processes which heavily depend on the seasonal monsoon, the El Niño/La Niña events, and the Indian Ocean Dipole (IOD). The results provide new insights into SCS dynamics from the point of view of ocean energy sources.

**Keywords:** available gravitational potential energy; mesoscale eddy; South China Sea; ENSO; IOD



**Citation:** Li, Q.; Zhou, L.; Xie, L. Seasonal and Interannual Variability of EAPE in the South China Sea Derived from ECCO2 Data from 1997 to 2019. *Water* **2021**, *13*, 926. <https://doi.org/10.3390/w13070926>

Academic Editor: Letizia Lusito

Received: 26 January 2021

Accepted: 24 March 2021

Published: 28 March 2021

**Publisher's Note:** MDPI stays neutral with regard to jurisdictional claims in published maps and institutional affiliations.



**Copyright:** © 2021 by the authors. Licensee MDPI, Basel, Switzerland. This article is an open access article distributed under the terms and conditions of the Creative Commons Attribution (CC BY) license (<https://creativecommons.org/licenses/by/4.0/>).

## 1. Introduction

Conservation of energy is a basic physical law that controls ocean circulation. Lorenz was a pioneer and established a four-box diagram for the energy budget in the atmosphere which is commonly known as the Lorenz energy cycle. By analogy, a lot of studies examined energy budgets in ocean contexts [1–7]; however, unlike the atmosphere, accumulating evidence indicates that the ocean is not a heat engine [8], i.e., the amplitude of ocean circulation is actually controlled by the mechanical energy, which is actually smaller than the surface heat flux into the ocean by a few order of magnitudes. The generation and accumulation of the available gravitational potential energy (APE) that is available for mixing and conversion into kinetic energy is an integral component of ocean dynamics [9,10]. Huang made a quantitative estimate of the APE for the world's oceans [11]. In recent years, eddy contribution to the APE, i.e., the eddy APE (EAPE), in open ocean areas has been investigated [12–15], while estimates of the EAPE are not widespread for marginal seas such as the South China Sea (SCS). This study aims to investigate the spatiotemporal variations of the EAPE in the SCS using the long-term and high-resolution reanalysis products.

As a large semi-enclosed marginal sea, the SCS features energetic mesoscale eddy processes due to the disturbances from the Pacific, seasonally reversed monsoons, the instability of local current, and the complex seafloor topography [16–22]. The statistical properties of eddies in the SCS have been presented in several studies [23–27] and recently reviewed by Zheng [28] and Lin [29]. The statistical results indicate that the numbers and shapes of two polarities of eddies are quite close. Their spatial and temporal scales were 132 km and 8.8 weeks, respectively, which was determined by relying on the locations where

the eddies were formed. The eddy propagation characteristics vary between locations in the SCS [24–26]. Temperature and thus density anomalies mostly extend vertically to 400–500 m, while salinity anomalies are apparent in the upper 150 m. Correspondingly, most heat and salt transport processes are concentrated in the upper 300 m and 100 m levels [25]. The eddy kinetic energy (EKE) in the SCS has also been intensively investigated [30–33]. The results show that the climatological mean EKE ranges from  $50 \text{ cm}^2/\text{s}^2$  to  $1400 \text{ cm}^2/\text{s}^2$  with a mean value of  $314 \text{ cm}^2/\text{s}^2$ . Spatially, the highest peak appears southeast of the Vietnam coast and the second highest one appears in the southwest of Taiwan. Seasonally, the mean EKE in spring, summer, autumn, and winter accounts for 19.4%, 26.6%, 29.3%, and 24.6% of the total, respectively. The seasonal cycle is a dominant mechanism controlling EKE variability east of the Vietnam coast, while the disturbances from the Pacific may be a leading cause of EKE variability southwest of Taiwan [31,32]. In addition to the seasonal variability, the mesoscale processes in the SCS also have pronounced interannual variability, which is largely attributed to the influence of El Niño–Southern Oscillation (ENSO) events [27,29,34,35] and the Indian Ocean Dipole (IOD) [36,37].

Energy budget analysis suggests that the release of APE is an important eddy energy source in the SCS [38]. Eddies also acquire/release kinetic energy mainly from/to the EAPE [39,40]; however, the detailed structure and variability of the EAPE in the SCS has not been well addressed. The next section gives descriptions of the data products and analysis methods. The results are presented in Section 3, including the climatological distributions, seasonal variability, and interannual variability. Discussion and conclusions are given in Sections 4 and 5, respectively.

## 2. Materials and Methods

The Estimating the Circulation and Climate of the Ocean, Phase II (ECCO2) reanalysis product from 1997 to 2019 as a baseline [41]. As an eddy-permitting model, ECCO2 has a spatial resolution of  $0.25^\circ$  latitude  $\times$   $0.25^\circ$  longitude, a time resolution of 3 days, and 50 vertical layers. Both the spatial and temporal resolutions are high enough to capture mesoscale eddies with radii larger than 60 km and lifetimes longer than 6 d. ECCO2 data have previously been used for the eddy energy budget analysis [42,43]. Since mesoscale eddies are generally larger than 200 km and last more than 60 days in the SCS [24,28], the ECCO2 data should be able to capture the main features of the EAPE.

The APE (denoted with  $P$ ) is calculated as per [42,43]:

$$P(x, y, z, t) = -\frac{g}{2n_0}(\rho - \langle \bar{\rho} \rangle)^2. \quad (1)$$

where  $g$  is the gravitational acceleration,  $\rho(x, y, z, t)$  is the density, and  $\langle \bar{\rho} \rangle$  is the reference state of the density, with the horizontal bar denoting a temporal average from 1997 to 2019, and  $\langle \cdot \rangle$  is the horizontal average over the whole SCS basin.  $n_0 = -\frac{\rho_0}{g} N_0^2$  denotes the stability of the reference state, where  $\rho_0 = \langle \bar{\rho} \rangle$  is the reference density and  $N_0 = \sqrt{-\frac{g}{\rho_0} \frac{d\rho_0}{dz}}$  is the mean buoyancy frequency derived from  $\rho_0$ . Hence,  $n_0$ ,  $\rho_0$ , and  $N_0$  are functions depth only. The mean APE (MAPE) is defined as

$$P_M(x, y, z) = -\frac{g}{2n_0} \left[ \overline{(\rho - \langle \bar{\rho} \rangle)} \right]^2. \quad (2)$$

The formula represents the mean APE in terms of time from its reference state. The EAPE is defined as

$$P_E(x, y, z, t) = -\frac{g}{2n_0}(\rho - \bar{\rho})^2. \quad (3)$$

The formula represents the APE anomalies stored in an instantaneous state with respect to the MAPE. The instantaneous state is referring to a 3-day snapshot of the ECCO2 data. For convenience, we defined  $\sigma = \rho - \bar{\rho}$ . As shown in the observation and model results, the eddy energy in the SCS is mainly confined to the upper layer of the ocean [25,44].

Thus, we integrated  $P_E(x, y, z, t)$  from the surface to 200 m to obtain the 2D ( $x, y$ ) distribution of the EAPE and MAPE in the following analysis.

The Niño 3.4 index was used for the interannual variability analysis in this study and features 3-month running mean sea surface temperature (SST) anomalies over the Niño 3.4 region within  $5^\circ \text{N}$ – $5^\circ \text{S}$  and  $120^\circ \text{W}$ – $170^\circ \text{W}$  [45]. The El Niño (La Niña) state is defined when the Niño 3.4 index is larger (smaller) than  $0.5^\circ \text{C}$  ( $-0.5^\circ \text{C}$ ). The IOD index defined in [46] was applied to separate the IOD phases, which are represented by the anomalous SST gradient between the western equatorial Indian Ocean ( $50^\circ \text{E}$ – $70^\circ \text{E}$  and  $10^\circ \text{S}$ – $10^\circ \text{N}$ ) and the southeastern equatorial Indian Ocean ( $90^\circ \text{E}$ – $110^\circ \text{E}$  and  $10^\circ \text{S}$ – $0^\circ \text{S}$ ). A positive (negative) IOD is defined as an IOD index larger (smaller) than its mean plus (minus) one standard deviation. A two-sample Student's  $t$ -test was applied to test the statistical significance between the ENSO phases and the IOD phases in the following analysis, assuming that the two samples have unknown and unequal variance.

### 3. Results

#### 3.1. Climatological Distribution

The 2D ( $x, y$ ) distribution of the MAPE and the climatological mean EAPE averaged from 1997 to 2019 in the SCS are shown in Figure 1a,b. One can see that the maximum values of the mean MAPE and EAPE are  $4 \times 10^4 \text{ J m}^{-2}$  and  $3 \times 10^4 \text{ J m}^{-2}$ , respectively. The total MAPE in the SCS is  $6.02 \times 10^4 \text{ J m}^{-2}$ , while the total EAPE is  $10.9 \times 10^4 \text{ J m}^{-2}$ . The EAPE accounts for 64% of the total APE (a sum of the MAPE and the EAPE) in the whole SCS, which is much larger than the estimated 20–30% for global oceans [6]. This is understandable, since eddies in the SCS are more energetic than in open oceans. Such evidence also indicates that the importance of the EAPE in global oceans may be underestimated, since the cases for marginal seas may be underestimated due to a lack of data.

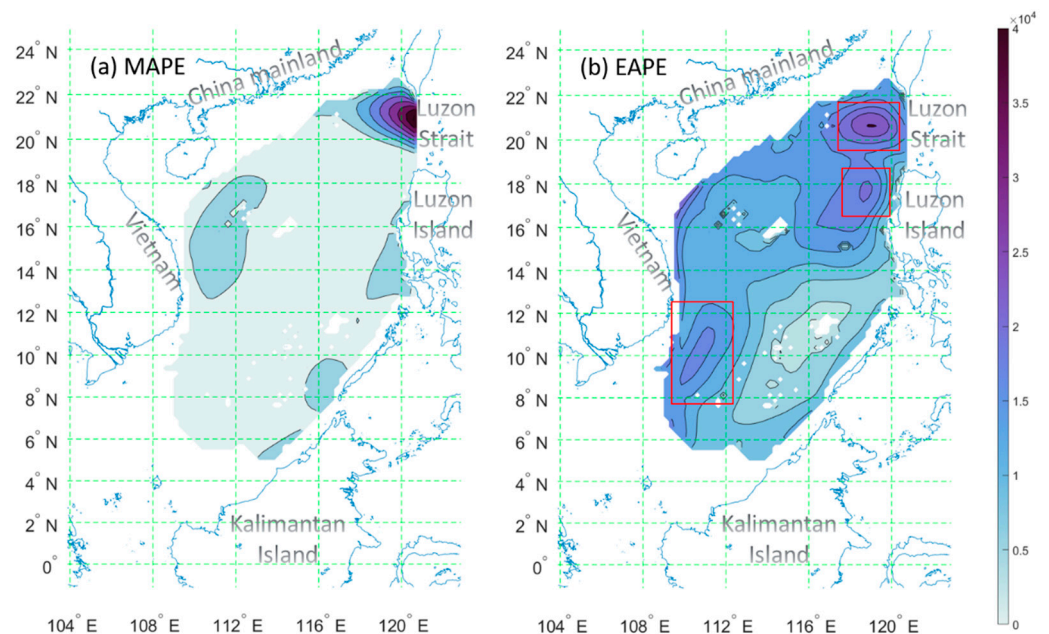


**Figure 1.** 2D distribution of the mean available gravitational potential energy (MAPE) (a) and climatological eddy available gravitational potential energy (EAPE) (b) in the SCS averaged from 1997 to 2019 and from the surface to 200 m. Units are  $\text{J m}^{-2}$ . Red boxes in (b) represent the three regions of peaked values.

As shown in Figure 1a, a high MAPE area with values above  $2 \times 10^4 \text{ J m}^{-2}$  originates from the Luzon Strait and extends westward to the northern SCS. In other regions, the MAPE values are generally uniform with values one order smaller, except the region off

the Vietnam coast, where the moderate MAPE of about  $1 \times 10^4 \text{ J m}^{-2}$  are distributed. In contrast to the highly concentrated distribution of high MAPE values, the EAPE features three peaked-value regions as shown in Figure 1b. Two regions are located in the northern SCS, where a northern one is centered around  $21^\circ \text{ N}$  near Luzon Strait and a southern one is centered around  $17^\circ \text{ N}$  and west of the Luzon Island. The two regions are consistent with the distribution of mesoscale eddies observed by satellite altimeter sea surface height (SSH) data [23]. The northern high EAPE region around  $21^\circ \text{ N}$  corresponds to the westward propagation path of eddies and disturbances originating from the northwest Pacific and entering the SCS [18,28,33,47,48]. The southern high EAPE region around  $17^\circ \text{ N}$  corresponds to the location of the periodic Luzon cold/warm eddy [49,50], consistent with the eddy train and the intrinsic basin normal modes in the basin [19,51,52]. The third high EAPE region is located off the Vietnam coast, where active coastal upwelling, eddy dipole, submesoscale vortices, and a western boundary current are present [53,54].

As indicated by Equation (3), the values of the EAPE depend on the density anomaly  $\sigma$  and the stratification  $N^2$ . Figure 2a,b shows the climatological distributions of  $\sigma$  and  $\log_{10} N^2$  in the SCS, respectively. One can see that a higher EAPE is generally consistent with a higher  $\sigma$  and lower  $N^2$ . The correlation coefficients  $R^2$  of the EAPE to  $\sigma^2$  and  $(N^2)^{-1}$ , respectively. From Figure 2c,d, one can see that in most areas of the SCS, the correlation coefficients of the EAPE to  $\sigma^2$ , i.e.,  $R_{\sigma}^2$ , are higher than 0.8, while those to  $(N^2)^{-1}$ , i.e.,  $R_N^2$ , are mostly lower than 0.3 in the central basin. In the northern boundary,  $R_N^2$  increases to over 0.6. Combined with the distributions of  $\sigma$  and  $\log_{10} N^2$ , we obtained the following understandings: 1) In the high EAPE region around  $21^\circ \text{ N}$ , there are higher density anomalies ( $\sigma > 3 \times 10^{-3} \text{ kg m}^{-3}$ ), and lower stratification ( $N^2 < 1 \times 10^{-3.8} \text{ s}^{-2}$ ).  $R_{\sigma}^2$  and  $R_N^2$  are both around 0.5. Both density anomalies and stratifications are dominant for higher EAPE values. 2) In the high EAPE area around  $17^\circ \text{ N}$ , since the density is dramatically disturbed with  $\sigma > 3.5 \times 10^{-3} \text{ kg m}^{-3}$  and  $R_{\sigma}^2 > 0.9$ , the EAPE is more affected by the disturbance of density. 3) In the high EAPE area off the coast of Vietnam, the disturbance of density plays a vital role in generating high EAPE values. Due to the larger stratification ( $N^2 > 1 \times 10^{-3.5} \text{ s}^{-2}$ ), the climatological mean EAPE in the western SCS is not as large as near the Luzon Strait and Luzon Island in the northern SCS as shown in Figure 1b.

### 3.2. Seasonal Variability

As shown in the above section, the EAPE distributions are highly correlated to the circulation in the SCS. Driven by the seasonal-reversed monsoon and the Kuroshio intrusion from the Luzon Strait, the SCS upper ocean circulation changes between two opposite gyres embedded with eddies, i.e., a cyclonic gyre is formed in winter while an anticyclonic gyre is formed in the southern SCS in summer [55,56]. During the transition period, dipole structures may be formed southeast from Vietnam as a cold tongue develops. Moreover, the seasonal variation is modulated by the interannual variations, which would affect the interannual variability of the EAPE.

Figure 3a–d shows the seasonal variability of the 2D EAPE distribution in the SCS. One can see that the general EAPE distribution pattern in spring (March, April and May, MAM) is similar with that in autumn (September October and November, SON), of which three peak EAPE regions align along the central line of the NE–SW basin. The pattern differs in summer (June, July and August, JJA) and winter (December, January and February, DJF), where the second peak region is located eastward near Luzon Island as per the climatological pattern in Figure 1b. The averaged EAPE of the whole SCS is  $1.09 \times 10^4 \text{ J m}^{-2}$  in winter, larger than the values of  $0.76 \times 10^4$ ,  $0.82 \times 10^4$ , and  $0.85 \times 10^4$  in spring, summer, and autumn, respectively.



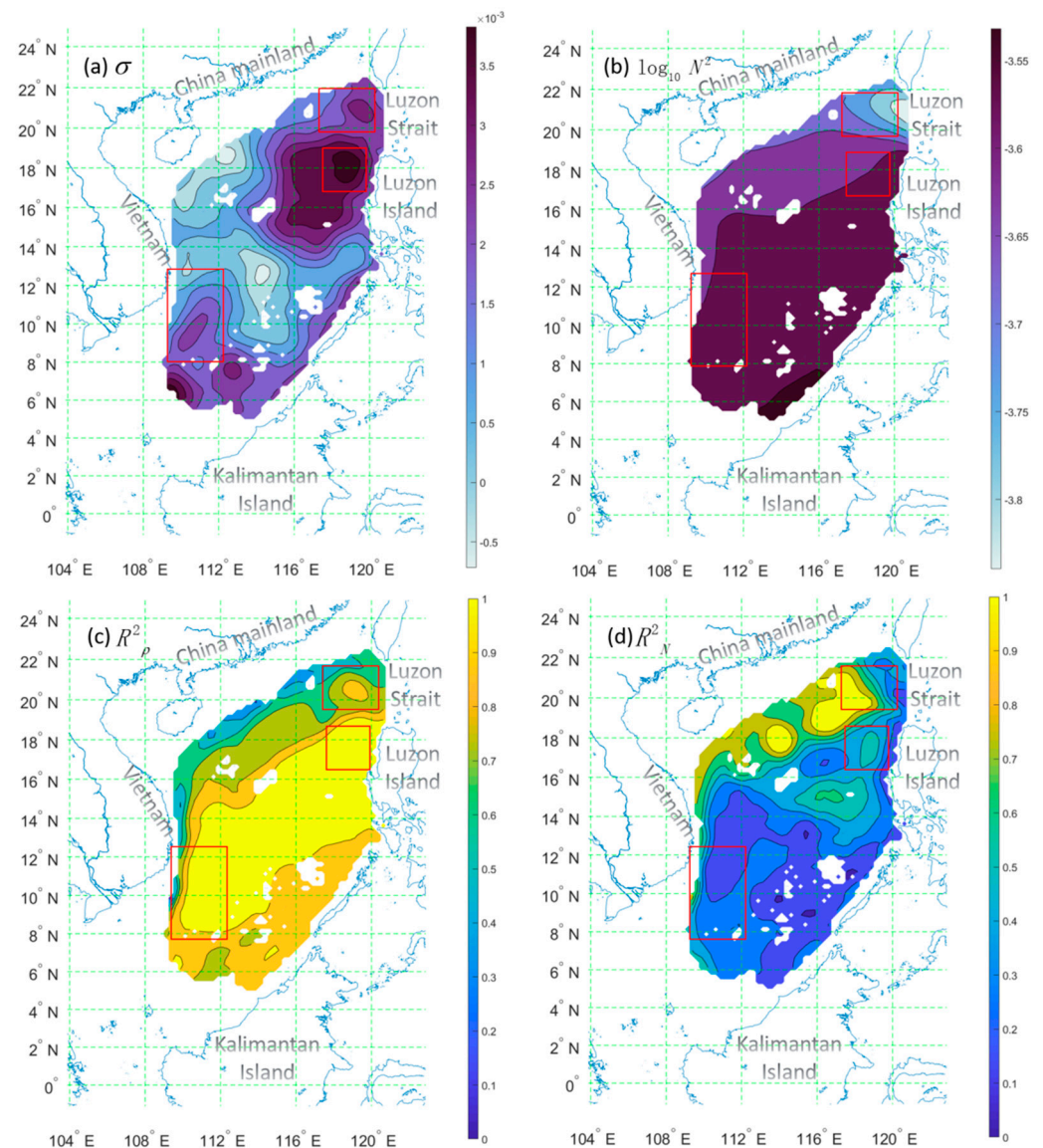


**Figure 2.** 2D distribution of climatological density anomalies  $\sigma$  (a,  $\text{kg m}^{-3}$ ) and stratifications  $\log_{10} N^2$  (b,  $\text{s}^{-2}$ ) and the correlation coefficients of EAPE to  $\sigma^2$  (c) and  $(N^2)^{-1}$  (d), respectively. Red boxes represent the three regions of peak values.

Table 1 shows the variation of the EAPE, density anomaly  $\sigma$  and stratification  $N^2$  in the three peak regions. One can see that in the region around  $21^\circ \text{N}$ , the EAPE has the largest value of  $1.83 \times 10^4 \text{ J m}^{-2}$  in winter and the lowest value of  $1.14 \times 10^4 \text{ J m}^{-2}$  in autumn. The annual mean EAPE here is  $1.41 \times 10^4 \text{ J m}^{-2}$  with a seasonal deviation of 21%, mostly due to the variation of stratification. Comparing to the other two regions, the stratifications and seasonal deviations of  $|\sigma|$  are the weakest here. For the region around  $17^\circ \text{N}$ , the EAPE reaches its maximum in winter and minimum in spring, with values between  $1.73 \times 10^4 \text{ J m}^{-2}$  and  $1.01 \times 10^4 \text{ J m}^{-2}$ , respectively. The values of  $\sigma^2$  in summer are 1.4 times higher than those in winter, but the maximum EAPE appears in winter due to weaker stratification. The high core of the EAPE shrinks and moves away from the coast. As a result, the EAPE reaches its minimum in spring when the periodic eddy and the wind stress are weak during the period of monsoon reversion [14,49]. Off the Vietnam coast in the western SCS, the northeasterly monsoon drives coastal downwelling in winter and spring. In contrast, the southwesterly monsoon drives water away from the coast and leads to strong coastal upwelling in summer and autumn [52], thus generating

submesoscale vortices [53]. Different from the two northern regions, the density anomaly  $\sigma$  off the Vietnam coast has large positive value over  $0.5 \text{ kg m}^{-3}$  in autumn due to the upwelling. Consequently, the EAPE here is enhanced and close to the highest value of  $1.22 \times 10^4 \text{ J m}^{-2}$  in winter as induced by weak stratification.

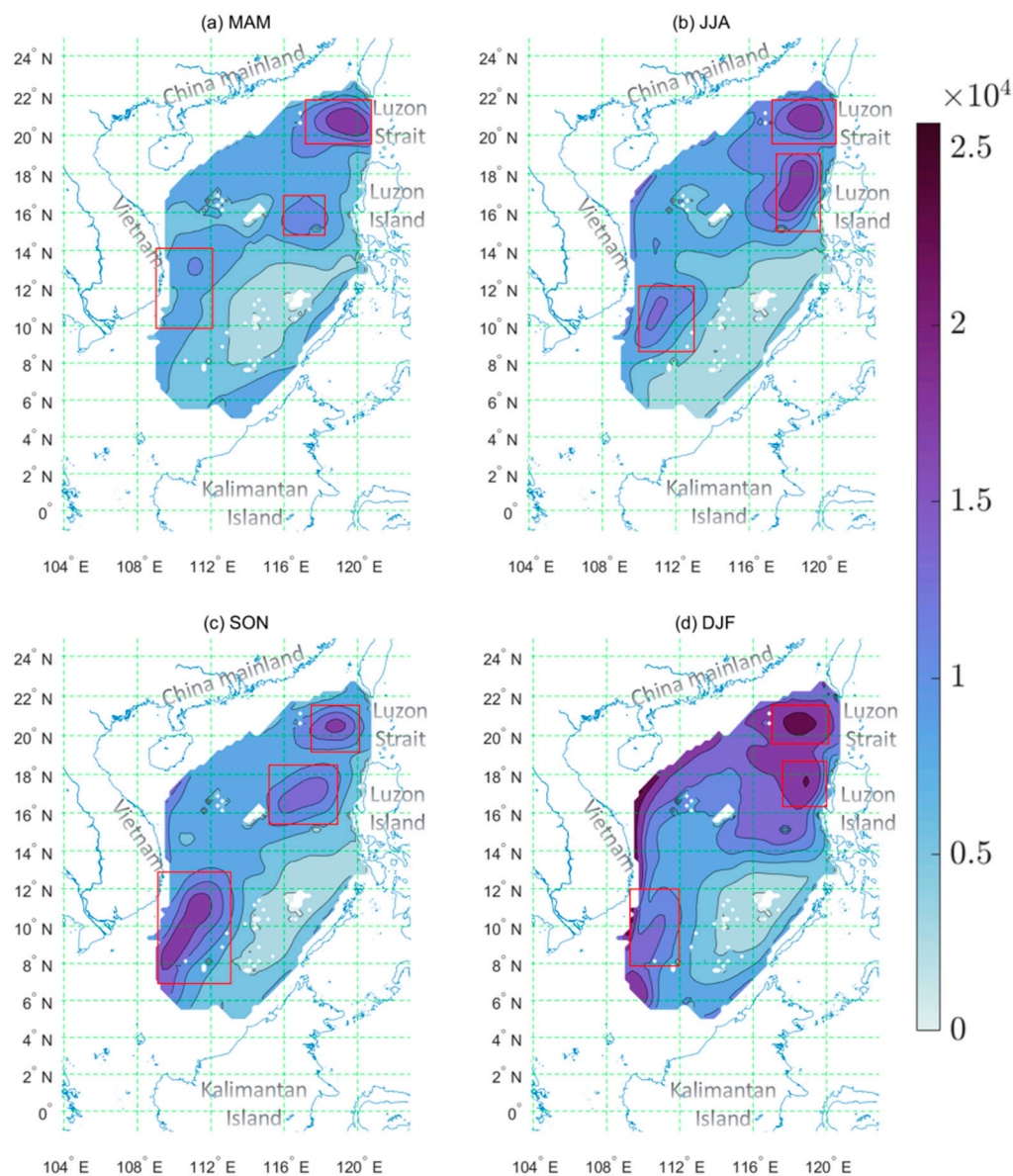


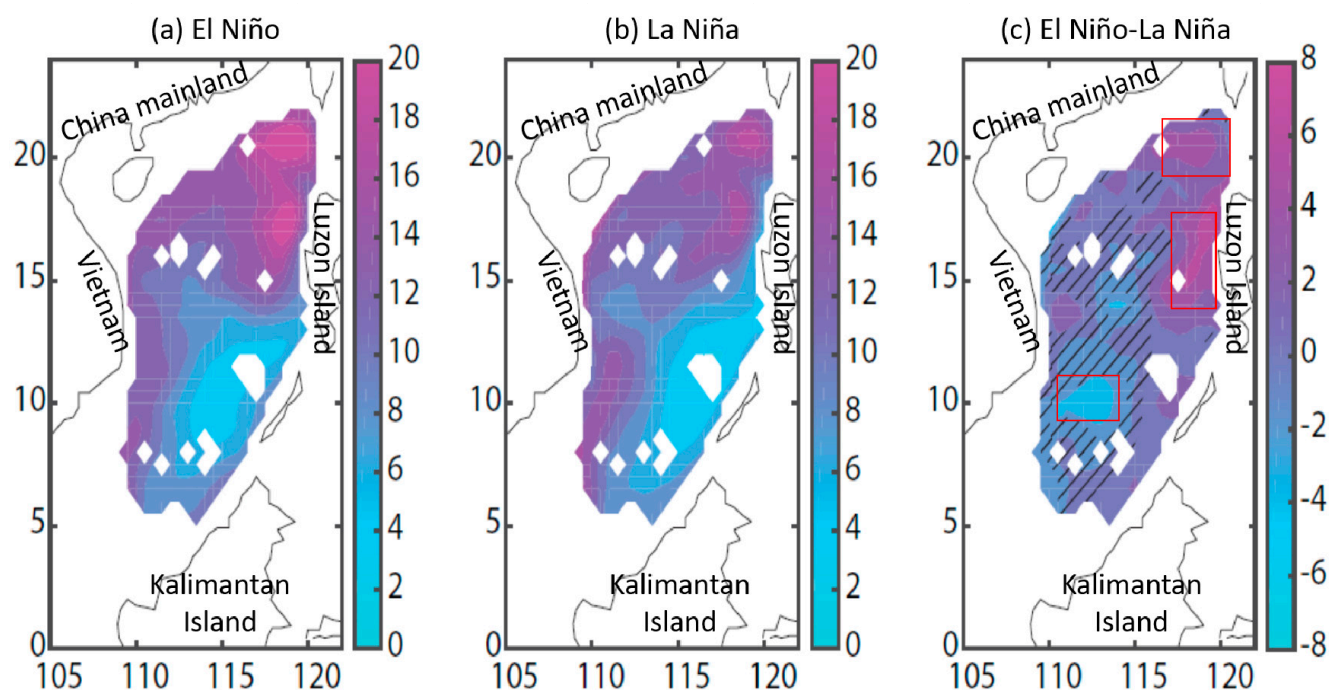
**Figure 3.** Mean EAPE values for March–May (a), June–August (b), September–November (c), and December–February (d). All results are averaged from 1997 to 2019 and integrated from the surface to 200 m. Units are  $\text{J m}^{-2}$ . Red boxes represent the three regions of peaked values.

### 3.3. Interannual Variability

Besides the seasonal variation, the EAPE in the SCS also manifests interannual variability due to the impacts of the ENSO and IOD. As shown in Figure 4, in the northern region around  $21^\circ \text{ N}$ , the EAPE is significantly higher during the El Niño events than that during the La Niña events. From the EAPE images shown in Figure 4a,b, we found the maximum value to be 10% higher and the area is occupied by values over  $18 \text{ kJ m}^{-2}$ , i.e., the total value of EAPE during the El Niño events is as high as about 5.5 times than that during the La Niña events.

**Table 1.** Seasonal variability of averaged parameters in three high EAPE regions (boxes in Figure 3).

Season	Around 21°N and West of Luzon Strait			Around 17°N and West of Luzon Island			Off the Vietnam Coast		
	EAPE × 10 <sup>4</sup> J m <sup>−2</sup>	σ kg m <sup>−3</sup>	N <sup>2</sup> log <sub>10</sub> s <sup>−2</sup>	EAPE × 10 <sup>4</sup> J m <sup>−2</sup>	σ kg m <sup>−3</sup>	N <sup>2</sup> log <sub>10</sub> s <sup>−2</sup>	EAPE × 10 <sup>4</sup> J m <sup>−2</sup>	σ kg m <sup>−3</sup>	N <sup>2</sup> log <sub>10</sub> s <sup>−2</sup>
Spring (March–May)	1.33	0.22	−3.71	1.01	0.25	−3.59	0.84	−0.03	−3.60
Summer (June–August)	1.33	−0.21	−3.62	1.26	−0.44	−3.57	0.98	−0.20	−3.57
Autumn (September–November)	1.14	−0.21	−3.66	1.09	−0.28	−3.58	1.20	0.50	−3.55
Winter (December–February)	1.83	0.20	−3.82	1.73	0.37	−3.73	1.22	0.21	−3.62
Mean	1.41	0.21 <sup>1</sup>	−3.70	1.27	0.33 <sup>1</sup>	−3.62	1.06	0.23 <sup>1</sup>	−3.59
STD	0.30	0.01	0.09	0.32	0.09	0.08	0.18	0.20	0.03

<sup>1</sup> Mean of the absolute density anomaly |σ|.

**Figure 4.** Mean EAPE for El Niño (a) and La Niña (b) and the differences between El Niño and La Niña (c). Units are kJ m<sup>−2</sup>. The hatches in (c) denote differences that are not statistically significant at a 95% confidence level.

In order to explain the significant EAPE increase phenomenon in the SCS during the El Niño events we considered the following scenario. During the El Niño events, the westerly wind burst drives the warm SST to shift eastward from the warm western Pacific pool and the easterly trade winds become weaker. As a result, the westward North Pacific Current is reduced. After the bifurcation of the North Pacific Current near the Philippines, the northward Kuroshio branch is weaker [57]. Due to the reduced momentum of the Kuroshio Current, the mesoscale disturbances from the Pacific easily penetrate the Kuroshio Current, and enter the northern SCS through the Luzon Strait [18,33]. Thus, the EAPE becomes stronger as shown in Figure 4a,c. In contrast, during the La Niña events, the trade winds and the North Pacific Current are stronger than the cases during the El Niño events. Consequently, the Kuroshio Current is stronger, leading weaker EAPE in the SCS.

In the region around 17°N, comparing with the seasonality shown in Figure 3, one can conclude that the EAPE is more dominated by the seasonal variability than that influenced by the ENSO events. The EAPE off the Vietnam coast only has an interannual variability of 4 kJ m<sup>−2</sup>. Since the monsoon circulation is generally weaker during the El Niño events [58,59], the coastal upwelling driven by the southwesterly monsoon winds tends to be stronger during the La Niña events and the EAPE is enhanced as shown in Figure 4b.

In addition, the EAPE is significantly enhanced during negative IOD phases as shown in Figure 5. For the positive IOD, the cyclonic winds in the lower troposphere tend to



reduce the northeastward monsoon winds along the Vietnam coast (e.g., [37]), which decreases the EAPE. Consistently, for the negative IOD, more eddies are generated and far higher EAPE is generated in the western SCS.

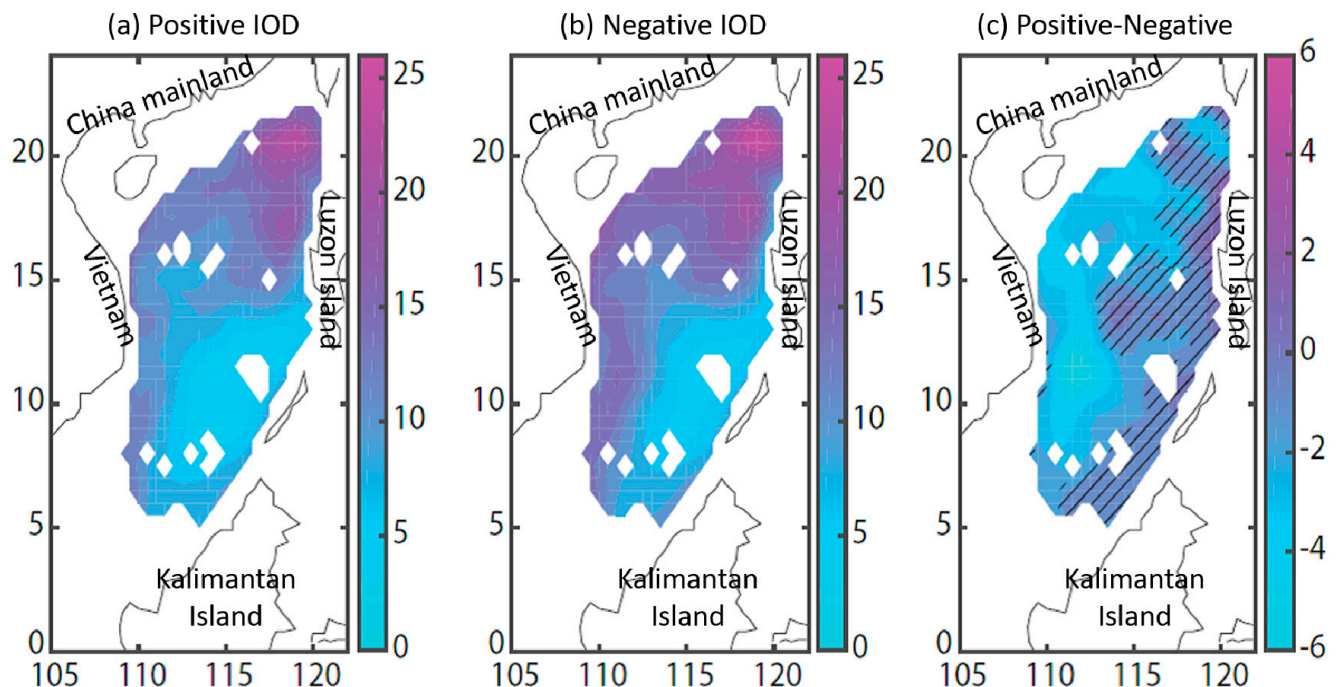


**Figure 5.** Same as Figure 4, but for the positive Indian Ocean Dipole (IOD) (a), negative IOD (b), and differences between the two IOD phases (c).

#### 4. Discussion

##### 4.1. Data Reanalysis

We have used ECCO2 data for EAPE analysis in this study. According to the inter-comparisons reported in [60], ECCO2 has the strongest mesoscale processes when comparing with other available reanalysis products (such as Simple Ocean Data Assimilation [61]). The eddy-resolving numerical model outputs may also be used for estimation, while the reanalysis data gathered directly from observations are prioritized for use. Considering the temporal and spatial resolutions of various ocean reanalysis products, ECCO2 is an applicable choice for the estimate of EAPE in the SCS.

Chen [42] compared ECCO2 data to observation data and found the misfits to be less than  $0.5\text{ }^{\circ}\text{C}$  for temperature and  $0.1\text{ psu}$  for salinity, respectively. Correspondingly, the density errors should be less than  $0.1\text{ kg m}^{-3}$  and the errors for the 200-m integrated APEs are less than  $20\text{ J m}^{-2}$  according to Equations (1)–(3). The APE errors are negligible when comparing to the values above  $1 \times 10^3\text{ J m}^{-2}$  in the results.

##### 4.2. Integral Depth

We applied a depth of 200 m as the integral limit for calculating the APE, though eddies may penetrate the whole depth of water in the SCS [44]. This is reasonable because the larger disturbance of eddies are mostly confined to the upper ocean [25]. Furthermore, the Brunt–Väisälä frequency, which determines the APE directly, reaches its maximum within a range from 50 to 75 m in the SCS [62,63]. The mixed layer in the SCS is mainly shallower than 100 m, implying that the APE is constrained to the upper ocean. Hence, setting the integral limit of the APE to 200 m is physically sound. In fact, we also calculated APE in the upper 1000 m and 3500 m levels, and the results (not shown) indicated similar distribution patterns with little differences in values.



#### 4.3. EKE and the EAPE

The EKE and the EAPE are two components of eddy mechanical energy. Previous studies have generally investigated the interactions between eddies and mean flow, while fewer studies have focused on the conversion between EAPE and EKE (i.e., [39]).

Using a high-resolution numerical model, Yang et al. investigated eddy energy sources and sinks in the SCS [38]. They found that over 60% (66%) of the EKE arises from EAPE releasing in winter (summer), indicating high EKE in the three high EAPE regions as shown in Figure 2. Kang et al. analyzed the eddy energy budget in the Gulf Stream region and found that the baroclinic conversion of APE→EAPE→EKE contributes 25% of the EKE [39]. Baroclinic instability and gravity play important roles in energy conversion.

Recently, Yang et al. [15] used a more advanced multiscale window transform (MWT) [64] method to examine the roles of multiscale interactions and instabilities in the context of loop current eddy shedding in the Gulf of Mexico and found that energy transform from APE to EKE plays an important role in the eddy shedding process. The MWT and canonical transfer theory [65] would be appropriate directions for more accurate energy budget calculation in ocean dynamics.

#### 5. Conclusions

In this study, the 2D distributions and temporal variability features of the EAPE in the SCS have been analyzed using state-of-the-art ECCO2 reanalysis products from 1997 to 2019. The major findings are summarized as follows:

1. The 2D distribution images of the climatological mean EAPE show that the higher EAPE values are distributed in three regions, where two regions are located in the northern SCS, with one around 21° N to the west of the Luzon Strait and the other one around 17° N near Luzon Island. The third region is in the western SCS off the coast of Vietnam.
2. The EAPE in the SCS presents an evident seasonal circle. The percentages of the seasonal EAPE over the total EAPE account for 21.6%, 23.2%, 24.2%, and 31.0% in spring, summer, autumn, and winter, respectively. A noticeable enhancement in winter is attributed to much weak stratification, especially in the northern SCS, which is favorable for enhancing the EAPE.
3. In the northern SCS, the EAPE is generally smaller in spring and autumn and larger in summer and winter. The location of the peak EAPE has little seasonal variation around 21° N but moves westward to the central basin around 17° N. For the interannual variability, the EAPE in the two northern regions weakens during La Nina periods. ENSO plays an important role in the northern SCS.
4. Off the Vietnam coast, the EAPE is closely related to coastal upwelling and presents higher values in autumn. The EAPE in this region has remarkable seasonal variabilities. During the La Niña events, the EAPE is enhanced and spreads from the Vietnam coast to the central SCS. During El Niño events, coastal upwelling and the EAPE are greatly suppressed. During the negative phase of the IOD, the EAPE is significantly enhanced in the western SCS, while there is no significant difference in the eastern SCS between the two IOD phases.

The above findings provide new insights into SCS dynamics from the point of view of ocean energy sources. In particular, the implications of the findings in exploring SCS response to climate change are worth further study.

**Author Contributions:** Q.L.: data acquisition, data analysis, visualization, writing—original draft preparation; L.Z.: data interpretation, visualization, writing—review and editing; L.X.: study design, data interpretation, writing—review and editing. All authors have read and agreed to the published version of the manuscript.

**Funding:** This research was funded by the IPOVAR Project (GASI-IPOVAI-01-02), the National Natural Science Foundation of China (41776034 and 411706025), and the Guangdong Province First-Class Discipline Plan (CYL231419012) and 231389002.

**Data Availability Statement:** The ECCO2 data used in this article were downloaded from <https://ecco.jpl.nasa.gov/drive/files/ECCO2> (accessed on 26 March 2021).

**Conflicts of Interest:** The authors declare no conflict of interest.

## References

- Holton, J.R. An introduction to dynamic meteorology. *Am. J. Phys.* **1973**, *41*, 752–754. [\[CrossRef\]](#)
- Lorenz, E.N. Available potential energy and the maintenance of the general circulation. *Tellus* **1955**, *7*, 157–167. [\[CrossRef\]](#)
- Tailleux, R. Available potential energy and exergy in stratified fluids. *Annu. Rev. Fluid Mech.* **2013**, *45*, 35–58. [\[CrossRef\]](#)
- Ferrari, R.; Wunsch, C. Ocean circulation kinetic energy: Reservoirs, sources, and sinks. *Annu. Rev. Fluid Mech.* **2009**, *41*. [\[CrossRef\]](#)
- Munk, W.; Wunsch, C. Abyssal recipes II: Energetics of tidal and wind mixing. *Deep Sea Res. Part I Oceanogr. Res. Pap.* **1998**, *45*, 1977–2010. [\[CrossRef\]](#)
- Oort, A.H.; Anderson, L.A.; Peixoto, J.P. Estimates of the energy cycle of the oceans. *J. Geophys. Res. Ocean.* **1994**, *99*, 7665–7688. [\[CrossRef\]](#)
- Wunsch, C.; Ferrari, R. Vertical mixing, energy, and the general circulation of the oceans. *Annu. Rev. Fluid Mech.* **2004**, *36*, 281–314. [\[CrossRef\]](#)
- Huang, R.X. Ocean, energy flows. *Encycl. Energy* **2004**, *4*, 497–509.
- Wunsch, C. What is the thermohaline circulation? *Science* **2002**, *298*, 1179–1181. [\[CrossRef\]](#)
- Huang, R.X. Mixing and available potential energy in a Boussinesq ocean. *J. Phys. Oceanogr.* **1998**, *28*, 669–678. [\[CrossRef\]](#)
- Huang, R.X. Available potential energy in the world's oceans. *J. Mar. Res.* **2005**, *63*, 141–158. [\[CrossRef\]](#)
- Luecke, C.; Arbic, B.; Bassette, S.; Richman, J.; Shriver, J.; Alford, M.; Smedstad, O.; Timko, P.; Trossman, D.; Wallcraft, A. The global mesoscale eddy available potential energy field in models and observations. *J. Geophys. Res. Ocean.* **2017**, *122*, 9126–9143. [\[CrossRef\]](#)
- Yang, Y.; Liang, X.S. The instabilities and multiscale energetics underlying the mean-interannual-eddy interactions in the Kuroshio Extension region. *J. Phys. Oceanogr.* **2016**, *46*, 1477–1494. [\[CrossRef\]](#)
- Yang, Y.; Liang, X.S.; Qiu, B.; Chen, S. On the decadal variability of the eddy kinetic energy in the Kuroshio Extension. *J. Phys. Oceanogr.* **2017**, *47*, 1169–1187. [\[CrossRef\]](#)
- Yang, Y.; Weisberg, R.H.; Liu, Y.; Liang, X.S. Instabilities and multiscale interactions underlying the loop current eddy shedding in the Gulf of Mexico. *J. Phys. Oceanogr.* **2020**, *50*, 1289–1317. [\[CrossRef\]](#)
- Hu, J.; Zheng, Q.; Sun, Z.; Tai, C.K. Penetration of nonlinear Rossby eddies into South China Sea evidenced by cruise data. *J. Geophys. Res. Ocean.* **2012**, *117*. [\[CrossRef\]](#)
- Xie, L.; Zheng, Q. New insight into the South China Sea: Rossby normal modes. *Acta Oceanol. Sin.* **2017**, *36*, 1–3. [\[CrossRef\]](#)
- Xie, L.; Zheng, Q.; Li, J.; Li, M.; Ho, C.-R. Responses of the South China Sea to mesoscale disturbances from the Pacific. *Reg. Oceanogr. South China Sea* **2020**, *10*, 243–287.
- Xie, L.; Zheng, Q.; Zhang, S.; Hu, J.; Li, M.; Li, J.; Xu, Y. The Rossby normal modes in the South China Sea deep basin evidenced by satellite altimetry. *Int. J. Remote Sens.* **2018**, *39*, 399–417. [\[CrossRef\]](#)
- Yuan, D.; Han, W.; Hu, D. Anticyclonic eddies northwest of Luzon in summer–fall observed by satellite altimeters. *Geophys. Res. Lett.* **2007**, *34*. [\[CrossRef\]](#)
- Zhang, Z.; Zhao, W.; Qiu, B.; Tian, J. Anticyclonic eddy sheddings from Kuroshio loop and the accompanying cyclonic eddy in the northeastern South China Sea. *J. Phys. Oceanogr.* **2017**, *47*, 1243–1259. [\[CrossRef\]](#)
- Zheng, Q.; Tai, C.-K.; Hu, J.; Lin, H.; Zhang, R.-H.; Su, F.-C.; Yang, X. Satellite altimeter observations of nonlinear Rossby eddy–Kuroshio interaction at the Luzon Strait. *J. Oceanogr.* **2011**, *67*, 365–376. [\[CrossRef\]](#)
- Wang, G.; Su, J.; Chu, P.C. Mesoscale eddies in the South China Sea observed with altimeter data. *Geophys. Res. Lett.* **2003**, *30*. [\[CrossRef\]](#)
- Chen, G.; Hou, Y.; Chu, X. Mesoscale eddies in the South China Sea: Mean properties, spatiotemporal variability, and impact on thermohaline structure. *J. Geophys. Res. Ocean.* **2011**, *116*. [\[CrossRef\]](#)
- He, Q.; Zhan, H.; Cai, S.; He, Y.; Huang, G.; Zhan, W. A new assessment of mesoscale eddies in the South China Sea: Surface features, three-dimensional structures, and thermohaline transports. *J. Geophys. Res. Ocean.* **2018**, *123*, 4906–4929. [\[CrossRef\]](#)
- Huang, R.; Xie, L.; Zheng, Q.; Li, M.; Bai, P.; Tan, K. Statistical analysis of mesoscale eddy propagation velocity in the South China Sea deep basin. *Acta Oceanol. Sin.* **2020**, *39*, 91–102. [\[CrossRef\]](#)
- Xiu, P.; Chai, F.; Shi, L.; Xue, H.; Chao, Y. A census of eddy activities in the South China Sea during 1993–2007. *J. Geophys. Res. Ocean.* **2010**, *115*. [\[CrossRef\]](#)
- Zheng, Q.; Xie, L.; Zheng, Z.; Hu, J. Progress in research of mesoscale eddies in the South China Sea. *Adv. Mar. Sci.* **2017**, *35*, 131–158.
- Lin, H.; Liu, Z.; Hu, J.; Menemenlis, D.; Huang, Y. Characterizing meso-to submesoscale features in the South China Sea. *Prog. Oceanogr.* **2020**, *188*, 102420. [\[CrossRef\]](#)
- Chen, G.; Hou, Y.; Chu, X.; Qi, P.; Hu, P. The variability of eddy kinetic energy in the South China Sea deduced from satellite altimeter data. *Chin. J. Oceanol. Limnol.* **2009**, *27*, 943. [\[CrossRef\]](#)
- Cheng, X.; Qi, Y. Variations of eddy kinetic energy in the South China Sea. *J. Oceanogr.* **2010**, *66*, 85–94. [\[CrossRef\]](#)

32. Sun, Z.; Zhang, Z.; Zhao, W.; Tian, J. Interannual modulation of eddy kinetic energy in the northeastern South China Sea as revealed by an eddy-resolving OGCM. *J. Geophys. Res. Ocean.* **2016**, *121*, 3190–3201. [\[CrossRef\]](#)
33. Zheng, Q.; Ho, C.-R.; Xie, L.; Li, M. A case study of a Kuroshio main path cut-off event and impacts on the South China Sea in fall-winter 2013–2014. *Acta Oceanol. Sin.* **2019**, *38*, 12–19. [\[CrossRef\]](#)
34. Fang, G.; Chen, H.; Wei, Z.; Wang, Y.; Wang, X.; Li, C. Trends and interannual variability of the South China Sea surface winds, surface height, and surface temperature in the recent decade. *J. Geophys. Res. Ocean.* **2006**, *111*. [\[CrossRef\]](#)
35. Tuo, P.; Yu, J.-Y.; Hu, J. The changing influences of ENSO and the Pacific meridional mode on mesoscale eddies in the South China Sea. *J. Clim.* **2019**, *32*, 685–700. [\[CrossRef\]](#)
36. Li, C.; Mu, M. The influence of the Indian Ocean dipole on atmospheric circulation and climate. *Adv. Atmos. Sci.* **2001**, *18*, 831–843.
37. Guan, Z.; Yamagata, T. The unusual summer of 1994 in East Asia: IOD teleconnections. *Geophys. Res. Lett.* **2003**, *30*. [\[CrossRef\]](#)
38. Yang, H.; Wu, L.; Liu, H.; Yu, Y. Eddy energy sources and sinks in the South China Sea. *J. Geophys. Res. Ocean.* **2013**, *118*, 4716–4726. [\[CrossRef\]](#)
39. Kang, D.; Curchitser, E.N. Energetics of Eddy-Mean Flow Interactions in the Gulf Stream Region. *Am. Geophys. Union* **2016**. [\[CrossRef\]](#)
40. Zhan, P.; Subramanian, A.C.; Yao, F.; Kartadikaria, A.R.; Guo, D.; Hoteit, I. The eddy kinetic energy budget in the Red Sea. *J. Geophys. Res. Ocean.* **2016**, *121*, 4732–4747. [\[CrossRef\]](#)
41. Menemenlis, D.; Campin, J.-M.; Heimbach, P.; Hill, C.; Lee, T.; Nguyen, A.; Schodlok, M.; Zhang, H. ECCO2: High resolution global ocean and sea ice data synthesis. *Mercator Ocean Q. Newsl.* **2008**, *31*, 13–21.
42. Chen, R. Energy Pathways and Structures of Oceanic Eddies from the ECCO2 State Estimate and Simplified Models. Ph.D. Thesis, Massachusetts Institute of Technology, Cambridge, MA, USA, 2013.
43. Chen, R.; Flierl, G.R.; Wunsch, C. A description of local and nonlocal eddy-mean flow interaction in a global eddy-permitting state estimate. *J. Phys. Oceanogr.* **2014**, *44*, 2336–2352. [\[CrossRef\]](#)
44. Zhang, Z.; Tian, J.; Qiu, B.; Zhao, W.; Chang, P.; Wu, D.; Wan, X. Observed 3D structure, generation, and dissipation of oceanic mesoscale eddies in the South China Sea. *Sci. Rep.* **2016**, *6*, 1–11. [\[CrossRef\]](#)
45. Trenberth, K.E. The definition of el nino. *Bull. Am. Meteorol. Soc.* **1997**, *78*, 2771–2778. [\[CrossRef\]](#)
46. Saji, N.; Goswami, B.; Vinayachandran, P.; Yamagata, T. A dipole mode in the tropical Indian Ocean. *Nature* **1999**, *401*, 360–363. [\[CrossRef\]](#) [\[PubMed\]](#)
47. Xie, L.; Zheng, Q.; Tian, J.; Zhang, S.; Feng, Y.; Yi, X. Cruise observation of Rossby waves with finite wavelengths propagating from the Pacific to the South China Sea. *J. Phys. Oceanogr.* **2016**, *46*, 2897–2913. [\[CrossRef\]](#)
48. Zhuang, W.; Xie, S.P.; Wang, D.; Taguchi, B.; Aiki, H.; Sasaki, H. Intraseasonal variability in sea surface height over the South China Sea. *J. Geophys. Res. Ocean.* **2010**, *115*. [\[CrossRef\]](#)
49. Wang, G.; Chen, D.; Su, J. Winter eddy genesis in the eastern South China Sea due to orographic wind jets. *J. Phys. Oceanogr.* **2008**, *38*, 726–732. [\[CrossRef\]](#)
50. Chu, X.; Chen, G.; Qi, Y. Periodic Mesoscale Eddies in the South China Sea. *J. Geophys. Res. Ocean.* **2020**, *125*, e2019JC015139. [\[CrossRef\]](#)
51. Nan, F.; He, Z.; Zhou, H.; Wang, D. Three long-lived anticyclonic eddies in the northern South China Sea. *J. Geophys. Res. Ocean.* **2011**, *116*. [\[CrossRef\]](#)
52. Zheng, Q.; Hu, J.; Zhu, B.; Feng, Y.; Jo, Y.H.; Sun, Z.; Zhu, J.; Lin, H.; Li, J.; Xu, Y. Standing wave modes observed in the South China Sea deep basin. *J. Geophys. Res. Ocean.* **2014**, *119*, 4185–4199. [\[CrossRef\]](#)
53. Shen, Y.; Jing, Z.; Tan, K.; Xie, L. Comparison of the responses of the Qiongdong upwelling and the Vietnam coastal upwelling to super El Nino events. *Adv. Mar. Sci.* **2019**, *37*, 374–386.
54. Yu, J.; Zheng, Q.; Jing, Z.; Qi, Y.; Zhang, S.; Xie, L. Satellite observations of sub-mesoscale vortex trains in the western boundary of the South China Sea. *J. Mar. Syst.* **2018**, *183*, 56–62. [\[CrossRef\]](#)
55. Liu, Y.; Yuan, Y.; Su, J.; Jiang, J. Circulation in the South China Sea in summer of 1998. *Chin. Sci. Bull.* **2000**, *45*, 1648–1655. [\[CrossRef\]](#)
56. Weisberg, R.H. Patterns of upper layer circulation variability in the South China Sea from satellite altimetry using the self-organizing map. *Acta Oceanol. Sin.* **2008**, *1*.
57. Kashino, Y.; España, N.; Syamsudin, F.; Richards, K.J.; Jensen, T.; Dutrieux, P.; Ishida, A. Observations of the North Equatorial current, Mindanao current, and Kuroshio current system during the 2006/07 El Niño and 2007/08 La Niña. *J. Oceanogr.* **2009**, *65*, 325–333. [\[CrossRef\]](#)
58. Ju, J.; Slingo, J. The Asian summer monsoon and ENSO. *Q. J. R. Meteorol. Soc.* **1995**, *121*, 1133–1168. [\[CrossRef\]](#)
59. Wang, B.; Wu, R.; Lau, K. Interannual variability of the Asian summer monsoon: Contrasts between the Indian and the western North Pacific–East Asian monsoons. *J. Clim.* **2001**, *14*, 4073–4090. [\[CrossRef\]](#)
60. Zhang, M.; Zhou, L.; Fu, H.; Jiang, L.; Zhang, X. Assessment of intraseasonal variabilities in China Ocean Reanalysis (CORA). *Acta Oceanol. Sin.* **2016**, *35*, 90–101. [\[CrossRef\]](#)
61. Carton, J.A.; Giese, B.S. A reanalysis of ocean climate using Simple Ocean Data Assimilation (SODA). *Mon. Weather Rev.* **2008**, *136*, 2999–3017. [\[CrossRef\]](#)
62. Lü, H.; He, Y.; Shen, H.; Cui, L.; Dou, C.e. A new method for the estimation of oceanic mixed-layer depth using shipboard X-band radar images. *Chin. J. Oceanol. Limnol.* **2010**, *28*, 962–967. [\[CrossRef\]](#)

- 
63. Wang, G.; Qiao, F.; Dai, D.; Hou, Y. A possible generation mechanism of the strong current over the northwestern shelf of the South China Sea. *Acta Oceanol. Sin.* **2011**, *30*, 27. [[CrossRef](#)]
  64. Liang, X.S.; Anderson, D.G. Multiscale window transform. *Multiscale Model. Simul.* **2007**, *6*, 437–467. [[CrossRef](#)]
  65. Liang, X.S. Canonical transfer and multiscale energetics for primitive and quasigeostrophic atmospheres. *J. Atmos. Sci.* **2016**, *73*, 4439–4468. [[CrossRef](#)]